SCATTERING OF X-WAVES FROM A CIRCULAR DISK USING A TIME DOMAIN INCREMENTAL THEORY OF DIFFRACTION

A. M. Attiya and E. El-Diwany

Department of Microwave Engineering
Electronic Research Institute, Dokki
Giza, 12211, Egypt

A. M. Shaarawi [†]

The Physics Department
The American University in Cairo
P.O. Box 2511, Cairo 11511, Egypt

I. M. Besieris

The Bradley Department of Electrical and Computer Engineering
Virginia Polytechnic Institute and State University
Blacksburg, Virginia 24061, USA

Abstract—The diffraction and scattering of a first-order ultra-wideband TE X-wave by a perfectly conducting circular disk is investigated using an augmented time-domain incremental theory of diffraction. The analysis relies on a pulsed plane wave representation of the incident X-wave. The diffraction and scattering of each constituent pulsed plane wave component is calculated at the observation point. A subsequent azimuthal angular superposition yields the diffracted and scattered field due to the incident X-wave pulse. Making use of the localization and symmetry properties of the incident TE X-wave, a novel four-sensor correlated detection scheme is introduced which is particularly effective in detecting the edges of the scattering disk and has an exceptional resolving power.

[†] On leave from the Department of Engineering Physics and Mathematics, Faculty of Engineering, Cairo University, Giza 12211, Egypt

1   Introduction

2   The Incident Transverse Electric (TE) X-Wave

3   Scattering of TE X-Waves from a Perfectly Conducting Circular Disk Using a TD-ITD Approach

4   TD-ITD Results for the Diffraction of a TE X-Wave Normally Incident on a Perfectly Conducting Circular Disk

5   Four-Sensor Correlated Detection of X-Waves Scattered from a Circular Disk

6   Resolving Power of the Four-Sensor Scheme for an Incident TE X-Wave

7   Concluding Remarks

References

1. INTRODUCTION

Localized waves are ultra-wideband pulsed fields that propagate with little dispersion and exhibit extended focus depths [1–15]. Because of these properties, it is expected that such pulses can be employed in the detection of buried objects, high-resolution imaging, and identification of scattering structures [16]. Localized waves encompass a large number of known pulses that are essentially based on two types of solutions, namely focus wave modes (FWM) and X-waves [11]. To determine the effectiveness of using localized waves in the aforementioned applications, one has to study the scattering and diffraction of such pulses. In earlier work [16, 17], the diffraction of an electromagnetic X-wave by a perfectly conducting infinite wedge has been studied using the uniform theory of diffraction (UTD) [18, 19]. The results of that analysis have been extended to the scattering of an X-wave from a conducting circular disk [16, 17]. Although features of the scattered field calculated using the UTD appear to be quite acceptable, such an approach presents difficulties; specifically, the appearance of singularities at caustics and the formation of cylindrical diffracted wavefronts in the far field region [16, 17]. These difficulties arise because within the framework of the UTD the edges of the circular disk are effectively represented as a combination of infinite wedges

[18, 19]. This physically contradicts the finiteness of the size of the disk. For this reason, it is more appropriate to express the total diffracted field as a superposition of incremental diffracted fields due to each point on the edge plus a superposition of incremental physical optics scattered field due to each illuminated point on the surface of the body. This approach is based on the incremental theory of diffraction (ITD) developed by Tibero et al. [20–23]. The resulting incremental fields yield the same results as the UTD in the limit as the structure takes the form of an infinite wedge.

An X-wave can be expressed in terms of an azimuthal angular superposition of pulsed plane waves whose wave vectors form circular conic surface defined by the apex angle θ_0 [24]. If the spectral content of each pulsed plane wave component is restricted to high frequencies, then asymptotic techniques like the time-domain incremental theory of diffraction (TD-ITD) can be used to calculate the scattered field due to each individual component. After determining the scattering of each individual pulsed plane wave component, one can add up the contributions from all components incident at different azimuthal angles. It will be shown that the backscattered field due to an electromagnetic X-wave incident on a circular disk is free from singularities at caustics. Furthermore, unlike results based on the UTD, the wave front of the backscattered X-wave acquires a spherical shape as it travels away from the scattering structure.

The azimuthal symmetry of the scattered X-wave suggests that one can employ a correlated detection scheme, whereby multiple sensors are used to receive the backscattered signal. This scheme is highly sensitive in detecting the position of the edges of the scatterer. Consequently, one would expect that it would have high-resolution capabilities when the backscattered signal is produced by two disks placed close to each other. A study of a four-sensor correlated detection scheme shows that X-waves can be superior to regular pulsed plane waves when it comes to the discrimination between two scattering circular disks separated by a small distance.

Our aim in this work is to study the scattering of a transverse electric (TE) X-wave from a perfectly conducting circular disk using a TD-ITD approach. The incident TE X-wave is formulated in Section 2 and the scattered field is calculated in Section 3. Numerical examples demonstrating the effectiveness of the TD-ITD method are provided in Section 4. Taking into consideration the results of Section 4, we introduce a four-sensor correlated detection scheme that appears to be particularly effective in detecting the edges of a scattering disk. In Section 5, a four-sensor detected signal is simulated as the source of the X-wave sweeps the region containing the scattering disk. Subsequently,

in Section 6, it is shown that the scattering of X-waves from two nearby disks produces a four-sensor output having an exceptional resolving power in comparison with a regular pulsed plane wave. Comments and concluding remarks are provided in Section 7.

2. THE INCIDENT TRANSVERSE ELECTRIC (TE) X-WAVE

The incident transverse (azimuthal) electric field component of the first order X-wave can be written as an azimuthal angular superposition, viz., [16]

$$E_\phi^i(\rho, z, t) = \operatorname{Re}\left(\frac{Z_0 \sin\theta_0}{4\pi^2 c^2}\int\limits_0^{2\pi} d\phi_{inc}\vec{a}_\phi \cdot \vec{e}_i(\phi_{inc})\right.$$
$$\left.\int\limits_0^\infty d\omega\omega^3 e^{-\omega a_0/c}e^{j\omega((t-t_0)-(\vec{R}-\vec{R}_0)\cdot\vec{s}_i(\phi_{inc})/c)}\right), \quad (1)$$

where c and Z_0 denote the speed of light in vacuum and the intrinsic impedance of free space, respectively, and a_0 is a positive parameter. The polarization vector $\vec{e}_i(\phi_{inc})$ and the propagation direction vector $\vec{s}_i(\phi_{inc})$ of each azimuthal component have been chosen as follows:

$$\vec{e}_i(\phi_{inc}) = -\sin\phi_{inc}\vec{a}_x + \cos\phi_{inc}\vec{a}_y, \tag{2a}$$
$$\vec{s}_i(\phi_{inc}) = -\cos\phi_{inc}\sin\theta_0\vec{a}_x - \sin\phi_{inc}\sin\theta_0\vec{a}_y - \cos\theta_0\vec{a}_z, \tag{2b}$$
$$\vec{a}_\phi = -\sin\phi_0\vec{a}_x + \cos\phi_0\vec{a}_y. \tag{2c}$$

The expression given in Eq. (1) represents a ϕ-polarized X-wave pulse moving in the negative z-direction. The propagation unit vectors $\vec{s}_i(\phi_{inc})$ lie on a conic surface having an apex angle θ_0, known as the axicon angle. Each individual $\vec{s}_i(\phi_{inc})$ is characterized by the azimuthal angle ϕ_{inc} in a plane perpendicular to the axis of propagation of the X-wave and is inclined to the axis of propagation by an angle θ_0. The X-wave can, therefore, be perceived as consisting of azimuthally tilted pulsed plane wave components with propagation directions specified by $\vec{s}_i(\phi_{inc})$. The integration over ω in Eq. (1) yields

$$E_\phi^i(\rho, z, t) =$$
$$\operatorname{Re}\left(\frac{6Z_0\sin\theta_0}{4\pi^2 c^2}\int\limits_0^{2\pi}d\phi_{inc}\frac{\cos(\phi_{inc}-\phi_0)}{\left[(a_0/c)-j((t-t_0)-(\vec{R}-\vec{R}_0)\cdot\vec{s}_i(\phi_{inc})/c)\right]^4}\right). (3)$$
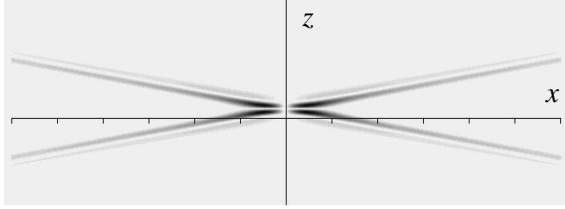
Figure 1. Incident first order TE X-wave ($x_0 = 0$, $y_0 = 0$, $z_0 = 10\,\text{cm}$); $a_0 = 10\,\text{cm}$, $\theta_0 = 10°$ and $t = 0\,\text{ns}$. The divisions along the ρ coordinate equal $50\,\text{cm}$.

The vector $\vec{R} = x\vec{a}_x + y\vec{a}_y + z\vec{a}_z$ specifies the observation point and $\vec{R}_0 = x_0\vec{a}_x + y_0\vec{a}_y + z_0\vec{a}_z$ corresponds to a reference point on the wavefront of the incident pulsed plane wave component at the initial time $t = t_0$. In addition, $\rho = \sqrt{(x - x_0)^2 + (y - y_0)^2}$, $\vec{\rho}_0 = x_0\vec{a}_x + y_0\vec{a}_y$, $\phi_0 = \tan^{-1}((y - y_0)/(x - x_0))$. An alternative representation for the incident X-wave field given in Eq. (1) is the following spectral superposition [16]:

$$\vec{E}^i(\vec{R}, t; \phi_{inc}) = \frac{Z_0 \sin\theta_0}{2\pi c^2}\text{Re}$$

$$\left[\int_0^\infty d\omega\,\omega^3 J_1((\omega/c)|\vec{\rho} - \vec{\rho}_0|\sin\theta_0)e^{-(\omega/c)a_0}e^{j\omega\{(t - t_0) - (z - z_0)\cos\theta_0/c\}}\vec{a}_\phi\right]. (4)$$

The incident first order TE X-wave is plotted in Fig. 1. A reference point at $t_0 = 0$ is ($x_0 = 0$, $y_0 = 0$, $z_0 = 10\,\text{cm}$). The parameters characterizing the incident field are $a_0 = 10\,\text{cm}$ and $\theta_0 = 10°$. The total field is normalized with respect to the peak value of the incident pulsed plane waves and is plotted using a sixteen-level grayscale. The divisions along the ρ coordinate equal $50\,\text{cm}$. The spectral amplitude of each azimuthally dependent pulsed component has the form $E_0(\omega) \propto \omega^3 \exp(-\omega a_0/c)$. This temporal spectral dependence has the advantage of allowing the derivation of closed form TD-ITD expressions for the diffracted pulsed plane wave components.

3. SCATTERING OF TE X-WAVES FROM A PERFECTLY CONDUCTING CIRCULAR DISK USING A TD-ITD APPROACH

In Ref. [25], a time-domain incremental theory of diffraction (TD-ITD) was formulated and applied to the scattering of pulsed plane waves

from a circular disk. In this section, that analysis will be extended to the scattering of a first order TE X-wave from a circular perfectly conducting disk. As discussed in Refs. [22] and [25], the ITD requires that one evaluates the physical optics, the shadow boundary line, and edge diffraction contributions to the scattered field. The last two have common characteristics and, hence, they are treated together. The physical optics part due to an incident X-wave can be obtained directly from the closed form expression of the field without the need to decompose the X-wave into a superposition of pulsed plane waves. This is due to the fact that the physical optics method depends on the tangential magnetic field or the current distribution at each point of the scattering body, which does not depend on the direction of incidence. This property is quite useful for saving the integration over the azimuthal directions of the pulsed plane wave components of the X-wave. However, both the shadow boundary line and the diffraction parts depend on the direction of the ray of incidence. Therefore, these two parts will be calculated using the pulsed plane wave representation of the X-wave [26].

3.1. The Physical Optics Field

The physical optics scattered field is determined using the surface electric current density on the scattering object. This current density is obtained from the tangential magnetic field on the surface. The spectral amplitude of the incident first order TE X-wave magnetic field at a scattering point is calculated as follows:

$$\vec{H}^i(\vec{R}, t) = (j/\omega\mu_0)\nabla \times \vec{E}^i(\vec{R}, t). \tag{5}$$

The spectral representation for the incident electric field given in Eq. (4) yields

$$
\begin{aligned}
\vec{H}^i(\vec{R}_s, \omega) &= H^i_\rho(\vec{R}_s, \omega)\vec{a}_\rho + H^i_z(\vec{R}_s, \omega)\vec{a}_z \\
&= \frac{j\omega^3}{2c^2}\sin\theta_0\cos\theta_0\exp(-a_0(\omega/c) \\
&\quad + j(z_s - z_0)(\omega/c)\cos\theta_0)J_1\left(|\vec{\rho}_s - \vec{\rho}_0|(\omega/c)\sin\theta_0\right)\vec{a}_\rho \\
&\quad + \frac{\omega^3}{2c^2}\sin^2\theta_0\exp(-a_0(\omega/c) \\
&\quad + j(z_s - z_0)(\omega/c)\cos\theta_0)J_0\left(|\vec{\rho}_s - \vec{\rho}_0|(\omega/c)\sin\theta_0\right)\vec{a}_z, \tag{6}
\end{aligned}
$$

where (x_0, y_0, z_0) is the center of the localization region of the incident X-wave at the starting time, $\vec{a}_\rho = \cos\phi_s\vec{a}_x + \sin\phi_s\vec{a}_y$, and $\phi_s = \tan^{-1}[(y_s - y_0)/(x_s - x_0)]$. The physical optics approximation of the

induced electric current on the surface of an electrically large scattering structure due to a magnetic field yields

$$\vec{J}(\vec{R}_s, \omega) = -2\vec{n} \times \vec{H}^i(\vec{R}_s, \omega) = -2\vec{a}_Z \times \vec{H}^i(\vec{R}_s, \omega), \qquad (7)$$

where $\vec{n}$ is the normal direction to the scattering surface at the scattering point which corresponds to the local Z direction at this point. In the far field region, the radiated electric field due to an infinitesimal current source is given by [27]:

$$\vec{E}(\vec{R}, \vec{R}_s, \omega) = -j(\omega/c)\frac{\exp(-j(\omega/c)|\vec{R}-\vec{R}_s|)}{4\pi|\vec{R} - \vec{R}_s|}Z_0\left[\vec{a}_R \times (\vec{a}_R \times \vec{J}(\vec{R}_s, \omega))\right]. \qquad (8)$$

Using Eqs. (7) and (8), it can be shown that the physical optics radiated electric amplitude due to an elementary point on the scattering structure can be expressed as a function of the incident magnetic field, viz.,

$$\vec{F}_s^{PO}(\vec{R}, \vec{R}_s, \omega) = \frac{-U(\pi/2 - \Theta')}{2\pi|\vec{R} - \vec{R}_s|}\vec{\vec{S}}_s^{PO}(\vec{R}_s)$$
$$\cdot \left(j(\omega/c)\exp(-j(\omega/c)|\vec{R} - \vec{R}_s|)Z_0\vec{H}^i(\vec{R}_s, \omega)\right), \qquad (9)$$

where $\vec{\vec{S}}_s^{PO}(\vec{R}_s)$ is the scattering dyadic expressed in terms of the local scattering spherical coordinates as follows:

$$\vec{\vec{S}}_s^{PO}(\vec{R}, \vec{R}_s) = \cos\Theta\sin\Phi\vec{a}_\Theta\vec{a}_X - \cos\Theta\cos\Phi\vec{a}_\Theta\vec{a}_Y$$
$$+ \cos\Phi\vec{a}_\Phi\vec{a}_X + \sin\Phi\vec{a}_\Phi\vec{a}_Y. \qquad (10)$$

The local Cartesian coordinates XYZ on the surface of the scattering body are defined so that the local Z direction is the normal to the scattering body and the X and Y coordinates are two arbitrary orthogonal tangential directions to the surface of the scattering structure at the scattering point $\vec{R}_s$. The coordinates (R, Θ, Φ) are the local spherical coordinates at the same point. It should be pointed out that the dyadic given in Eq. (10) is different from the one used in Eq. (3.2.c) of Ref. [25]. In that reference, the scattered field was derived in terms of the incident electric field expressed in the local spherical coordinates. In the present analysis, we prefer to express the incident magnetic field in terms of the local Cartesian coordinates at the scattering point. This can be done using the transformation

$$\begin{bmatrix} H_X^i \\ H_Y^i \\ H_Z^i \end{bmatrix} = \mathbf{\Pi} \begin{bmatrix} H_x^i \\ H_y^i \\ H_z^i \end{bmatrix} = \begin{bmatrix} \cos\nu & \sin\nu & 0 \\ -\sin\nu & \cos\nu & 0 \\ 0 & 0 & 1 \end{bmatrix} \begin{bmatrix} \cos\phi_s H_\rho^i \\ \sin\phi_s H_\rho^i \\ H_z^i \end{bmatrix}, \qquad (11)$$

where $0 \leq \nu \leq 2\pi$ specifies the azimuthal angle of different points on the surface of the disk. Following the analysis provided in Appendix I of Ref. [25] to relate the scattered field components transformed from the local spherical coordinates to the local Cartesian coordinates, we obtain

$$
\vec{\bar{S}}_s^{PO}(R_s) \cdot \vec{H}^i = \left[\mathbf{\Pi}^{-1}[P_2(\Theta, \Phi)] \begin{bmatrix} \cos\Theta\sin\Phi & -\cos\Theta\cos\Phi \\ \cos\Phi & \sin\Phi \end{bmatrix} \right.
$$
$$
\left. \begin{bmatrix} 1 & 0 & 0 \\ 0 & 1 & 0 \end{bmatrix} \mathbf{\Pi} \begin{bmatrix} \cos\phi_s H_\rho^i \\ \sin\phi_s H_\rho^i \\ H_z^i \end{bmatrix} \right]^T \begin{bmatrix} \vec{a}_x \\ \vec{a}_y \\ \vec{a}_z \end{bmatrix} \tag{12}
$$

The time-domain physical optics part due to an incident X-wave can be expressed as

$$
\vec{E}_s^{PO}(\vec{R}, t) = \iint\limits_S \vec{F}^{PO}(\vec{R}, \vec{R}_s, t) dS, \tag{13}
$$

where the elementary time domain physical optics field amplitude due to a point source on the surface of the scatterer is given by the analytic Fourier transform

$$
\vec{F}^{PO}(\vec{R}, \vec{R}_s, t) = \frac{1}{\pi} \mathrm{Re} \left\{ \int_0^\infty d\omega e^{j\omega t} \vec{F}^{PO}(\vec{R}, \vec{R}_s, \omega) \right\}
$$
$$
= \frac{-2Z_0 U(\pi/2 - \Theta')}{8\pi^2 c^3 |\vec{R} - \vec{R}_s|} \vec{\bar{S}}_s^{PO}(\vec{R}, \vec{R}_s) \cdot \vec{\aleph}(\vec{R}, \vec{R}_s, t), \tag{14a}
$$

where

$$
\vec{\aleph}(\vec{R}, \vec{R}_s, t) = \aleph_\rho(\vec{R}, \vec{R}_s, t) \left[\vec{a}_x \cos\phi_s + \vec{a}_y \sin\phi_s \right] + \aleph_z(\vec{R}, \vec{R}_s, t) \vec{a}_z. \tag{14b}
$$

The functions $\aleph_\rho(\vec{R}, \vec{R}_s, t)$ and $\aleph_z(\vec{R}, \vec{R}_s, t)$ acquire the following explicit form after a few manipulations:

$$
\aleph_\rho(\vec{R}, \vec{R}_s, t) = \sin\theta_0 \cos\theta_0 \mathrm{Re} \left[\frac{\partial^4}{\partial t^4} \frac{\sqrt{\beta^2(\vec{R}_s) + \alpha^2(\vec{R}, \vec{R}_s, t)} - \alpha(\vec{R}, \vec{R}_s, t)}{\beta(\vec{R}_s)\sqrt{\beta^2(\vec{R}_s) + \alpha^2(\vec{R}, \vec{R}_s, t)}} \right]
$$
$$
= \sin\theta_0 \cos\theta_0 \mathrm{Re} \left[15 \left(-\frac{3\alpha}{A^5} + \frac{10\alpha^3}{A^7} - \frac{7\alpha^5}{A^9} \right) \right], \tag{15a}
$$

$$\aleph_z(\vec{R}, \vec{R}_s, t) = \sin^2\theta_0 \mathrm{Re}\left[-j\frac{\partial^4}{\partial t^4}\frac{1}{\sqrt{\beta^2(\vec{R}_s) + \alpha^2(\vec{R}, \vec{R}_s, t)}}\right]$$

$$= \sin^2\theta_0 \mathrm{Re}\left[-j\left(\frac{105\alpha^4}{A^9} - \frac{90\alpha^2}{A^7} + \frac{9}{A^5}\right)\right]. \tag{15b}$$

Here

$$\alpha(\vec{R}, \vec{R}_s, t) = \left\{a_0 - j(ct - |\vec{R} - \vec{R}_s| + (z_s - z_0)\cos\theta_0)\right\}/c, \tag{15c}$$

$$\beta(\vec{R}_s) = (|\vec{\rho}_s - \vec{\rho}_0|\sin\theta_0)/c, \tag{15d}$$

and

$$A(\vec{R}, \vec{R}_s, t) = \sqrt{\beta^2(\vec{R}_s) + \alpha^2(\vec{R}, \vec{R}_s, t)}. \tag{15e}$$

These results have been obtained after applying identity (6.611.1) in Ref. [28]

$$\int_0^\infty J_\nu(\beta x)\exp[-\alpha x]dx = \frac{\beta^{-\nu}\left[\sqrt{\alpha^2 + \beta^2} - \alpha\right]^\nu}{\sqrt{\alpha^2 + \beta^2}},$$

$$\mathrm{Re}\,\nu > -1, \ \mathrm{Re}(\alpha \pm j\beta) > 0,$$

to evaluate the integration in (14a). Substituting in Eq. (13), we obtain the time-domain expression for the physical optics field.

3.2. The Shadow-Boundary-Line and the Edge-Diffracted Fields

The spectral components of the incident electric field of the first order TE X-wave can be considered as a superposition of obliquely incident plane waves in all azimuthal directions, as given in Eq. (1). Explicitly, we have the following spectral components incident on the diffraction edge:

$$\vec{E}^i(\vec{R}_e, \omega) = \frac{Z_0\sin\theta_0}{4\pi c^2}\int_0^{2\pi}d\phi_{inc}\omega^3 e^{-(\omega/c)[a_0 + j(\vec{R}_e - \vec{R}_0)\cdot\vec{s}_i(\phi_{inc})]}\vec{e}_i(\phi_{inc}). \tag{16}$$

Following the same analysis as that given in Ref. [25], the shadow-boundary-line and the edge-diffraction parts of the incident first order TE X-wave are given by the following azimuthal angular

superpositions:

$$\vec{F}_{SBL}^{PO}(\vec{R}, \vec{R}_{SBL}, t) = \frac{Z_0 \sin \theta_0}{8\pi^3 c^2} \frac{1}{|\vec{R} - \vec{R}_{SBL}|} \int\limits_0^{2\pi} d\phi_{inc}$$

$$\times \mathrm{Re} \left[\int\limits_0^\infty \omega^3 e^{-(\omega/c)[a_0 + j(ct - (\vec{R}_{SBL} - \vec{R}_0) \cdot \vec{s}_i(\phi_{inc}) - |\vec{R} - \vec{R}_{SBL}|)]} \right.$$

$$\left. \vec{\vec{S}}_{SBL}^{PO}(\vec{R}, \vec{R}_{SBL}, \omega) \cdot \vec{e}_i(\phi_{inc}) d\omega \right] \tag{17a}$$

$$\vec{F}^d(\vec{R}, \vec{R}_e, t) = \frac{Z_0 \sin \theta_0}{8\pi^3 c^2} \frac{1}{|\vec{R} - \vec{R}_e|} \int\limits_0^{2\pi} d\phi_{inc}$$

$$\times \mathrm{Re} \left[\int\limits_0^\infty \omega^3 e^{-(\omega/c)[a_0 + j(ct - (\vec{R}_e - \vec{R}_0) \cdot \vec{s}_i(\phi_{inc}) - |\vec{R} - \vec{R}_e|)]} \right.$$

$$\left. \vec{\vec{S}}^d(\vec{R}, \vec{R}_e, \omega) \cdot \vec{e}_i(\phi_{inc}) d\omega \right]. \tag{17b}$$

In these expressions, $\vec{\vec{S}}_{SBL}^{PO}(\vec{R}, \vec{R}_{SBL}, \omega) \cdot \vec{e}_i(\phi_{inc})$ and $\vec{\vec{S}}^d(\vec{R}, \vec{R}_e, \omega) \cdot \vec{e}_i(\phi_{inc})$ are determined for each azimuthal angle ϕ_{inc} using the incident polarization vector $\vec{e}_i(\phi_{inc})$ and the wave vector $\vec{s}_i(\phi_{inc})$ for each plane wave component, as discussed in Appendix II in Ref. [25]. Consequently, we obtain

$$\vec{F}_{SBL}^{PO}(\vec{R}, \vec{R}_{SBL}, t) = \frac{Z_0 \sin \theta_0}{8\pi^3 c^2 |\vec{R} - \vec{R}_{SBL}|} \int\limits_0^{2\pi} d\phi_{inc} \prod{}^{-1} [P_2(\beta, \varphi)]$$

$$\begin{bmatrix} \Sigma_{\beta\beta'}^{SBL}(\vec{R}, \vec{R}_{SBL}, t) & \Sigma_{\beta\varphi'}^{SBL}(\vec{R}, \vec{R}_{SBL}, t) \\ \Sigma_{\varphi\beta'}^{SBL}(\vec{R}, \vec{R}_{SBL}, t) & \Sigma_{\varphi\varphi'}^{SBL}(\vec{R}, \vec{R}_{SBL}, t) \end{bmatrix} \begin{bmatrix} e_\beta^i \\ e_\varphi^i \end{bmatrix} \tag{18a}$$

and

$$\vec{F}^d(\vec{R}, \vec{R}_e, t) = \frac{Z_0 \sin \theta_0}{8\pi^3 c^2 |\vec{R} - \vec{R}_e|} \int\limits_0^{2\pi} d\phi_{inc} \prod{}^{-1} [P_2(\beta, \varphi)]$$

$$\begin{bmatrix} \Xi_{\beta\beta'}^d(\vec{R}, \vec{R}_e, t) & \Xi_{\beta\varphi'}^d(\vec{R}, \vec{R}_e, t) \\ \Xi_{\varphi\beta'}^d(\vec{R}, \vec{R}_e, t) & \Xi_{\varphi\varphi'}^d(\vec{R}, \vec{R}_e, t) \end{bmatrix} \begin{bmatrix} e_\beta^i \\ e_\varphi^i \end{bmatrix}, \tag{18b}$$

where

$$\Sigma_{\beta\beta'}^{SBL} = \sum_{\ell=1}^{2} \text{Re}\left[I_2(\vec{R},t;X_\ell^{SBL},\phi_{inc})\right] L_\ell^E U(\pi - \varphi'), \quad (19a)$$

$$\Sigma_{\beta\varphi'}^{SBL} = -U(\pi - \varphi')\text{Re}[I_1(\vec{R},t,\phi_{inc})]\cos\beta, \quad (19b)$$

$$\Sigma_{\varphi\beta'}^{SBL} = 0, \quad (19c)$$

$$\Sigma_{\varphi\varphi'}^{SBL} = \sum_{\ell=1}^{2} \text{Re}\left[I_2(\vec{R},t;X_\ell^{SBL},\phi_{inc})\right] L_\ell^M U(\pi - \varphi'), \quad (19d)$$

and

$$\Xi_{\beta\beta'}^{d} = (1/n)\sum_{\ell=1}^{4} \text{Re}\left[I_2(\vec{R},t;X_\ell^e,\phi_{inc})\right] K_\ell^E, \quad (20a)$$

$$\Xi_{\beta\varphi'}^{d} = 0, \quad (20b)$$

$$\Xi_{\varphi\beta'}^{d} = 0, \quad (20c)$$

$$\Xi_{\varphi\varphi'}^{d} = (1/n)\sum_{\ell=1}^{4} \text{Re}\left[I_2(\vec{R},t;X_\ell^e,\phi_{inc})\right] K_\ell^M. \quad (20d)$$

The parameters K_ℓ^M, K_ℓ^E, L_ℓ^M and L_ℓ^E have the same definitions as in [25]. In the above expressions, the quantities $I_1(\vec{R},t)$ and $I_2(\vec{R},t;X_\ell^*)$ are given explicitly by

$$I_1(t,\vec{R},\phi_{inc}) = \int_0^\infty \omega^3 e^{-(\omega/c)[a_0 - j(ct - (\vec{R}_{SBL} - \vec{R}_0)\cdot\vec{s}_i(\phi_{inc}) - |\vec{R} - \vec{R}_{SBL}|)]} d\omega$$

$$= \frac{6}{\left[\left(a_0 - j(ct - (\vec{R}_{SBL} - \vec{R}_0)\cdot\vec{s}_i(\phi_{inc}) - |\vec{R} - \vec{R}_{SBL}|)\right)/c\right]^4} \quad (21)$$

and

$$I_2(t,\vec{R};X_\ell^*,\phi_{inc}) =$$
$$\frac{1}{2}\sqrt{\pi q(\vec{R})}\int_0^\infty \omega^3\sqrt{\omega}\,e^{-\omega[p(t,\vec{R},\phi_{inc}) - q(\vec{R})]} erfc\left(\sqrt{\omega q(\vec{R})}\right) d\omega, \quad (22a)$$

where

$$p(t,\vec{R},\phi_{inc}) = -j\left(\left(ct - (\vec{R}^* - \vec{R}_0)\cdot\vec{s}_i(\phi_{inc}) - |\vec{R} - \vec{R}^*|\right) + ja_0\right)/c, \quad (22b)$$

$$q(\vec{R}) = j\left(|\vec{R} - \vec{R}^*|\sin^2\beta_0\alpha_i(\varphi,\varphi')\right)/c. \quad (22c)$$

Here, Eqs. (10)–(14) and (18)–(20) have been used, while the asterisk in $\vec{R}^*$ and X_ℓ^* refers to either the edge or the shado-boundary-line. Notice that the integrand in (22a) differs from the corresponding one for pulsed plane waves [cf. Eq. (3.18a) in Ref. 25] by the quantity ω^3 which is equivalent to $j\partial^3/\partial t^3$. Therefore, Eq. (22a) can be rewritten as

$$I_2(t, \vec{R}, \phi_{inc}) = \frac{1}{2}\sqrt{\pi q(\vec{R})}\frac{j\partial^3}{\partial t^3}\int_0^\infty \sqrt{\omega}e^{-\omega[p(t,\vec{R},\phi_{inc})-q(\vec{R})]}erfc\left(\sqrt{\omega q(\vec{R})}\right)d\omega. \tag{23}$$

Using the result derived for a pulsed plane wave incident on a circular disk [25], it can be shown that the above integration reduces to

$$I_2(t, \vec{R}, \phi_{inc}) = \frac{1}{2q(\vec{R})}\frac{j\partial^3}{\partial t^3}\left[\frac{\tan^{-1}\sqrt{N(t,\vec{R},\phi_{inc})}}{(N(t,\vec{R},\phi_{inc}))^{3/2}}\right.$$
$$\left. - \frac{1}{N(t,\vec{R},\phi_{inc})(N(t,\vec{R},\phi_{inc})+1)}\right], \tag{24}$$

where $N(t, \vec{R}, \phi_{inc}) = (p(t, \vec{R}, \phi_{inc}) - q(\vec{R}))/q(\vec{R})$. Evaluating the dfferentiation in Eq. (24), it follows that

$$I_2(t, \vec{R}, \phi_{inc}) = \frac{-1}{2[q(\vec{R})]^4}\left[\frac{1}{N^2(N+1)}\left(\frac{7.125}{N^2} + \frac{2.75}{N(N+1)} + \frac{1}{(N+1)^2}\right)\right.$$
$$-13.125\frac{\tan^{-1}\sqrt{N}}{N^{4.5}} + \frac{6}{N(N+1)}$$
$$\left. \cdot \left(\frac{1}{N^3} + \frac{1}{N^2(N+1)} + \frac{1}{N(N+1)^2} + \frac{1}{(N+1)^3}\right)\right]. \tag{25}$$

Substituting Eqs. (21) and (25) into Eqs. (18)–(20), one can obtain the time domain shadow-boundary-line and the edge-diffracted field amplitudes after numerically evaluating the integrations over ϕ_{inc}. The total time-domain field is obtained by combining these two parts with the physical optics part given in Eqs. (14)–(15); specifically [22],

$$\vec{E}_s^{tot}(\vec{R}, t) = \iint_S \vec{F}_s^{PO}(\vec{R}, \vec{R}_s, t)dS$$
$$- \int_{SBL} \vec{F}_{SBL}^{PO}(\vec{R}, \vec{R}_{SBL}, t)dl + \int_e \vec{F}^d(\vec{R}, \vec{R}_e, t)dl. \tag{26}$$

4. TD-ITD RESULTS FOR THE DIFFRACTION OF A TE X-WAVE NORMALLY INCIDENT ON A PERFECTLY CONDUCTING CIRCULAR DISK

In this section, we shall discuss the backscattered field due to a first order TE X-wave normally incident on a perfectly conducting disk, which has been calculated by the TD-ITD method. Fig. 2 shows the ϕ-component of the total backscattered field for different initial locations of the X-wave localization region. The parameters characterizing the incident X-wave are $a_0 = 10\,\mathrm{cm}$ and $\theta_0 = 10°$. The backscattered fields are normalized to the peak value of the incident TE X-wave and are plotted using a sixteen-level gray-scale at $t = 6\,\mathrm{ns}$. The circular disk has a radius $L = 50\,\mathrm{cm}$, it lies on the xy plane with its center on the origin of the coordinate system. The axis of propagation of the X-wave passes through the points $x_0 = 0, 50, 75$ and $100\,\mathrm{cm}$. If these plots are compared to the scattered X-waves fields calculated using TD-UTD [17], one can conclude that the results obtained using TD-ITD show more continuity. This behavior is not only due to modifications in the calculation of the diffraction part of the field, but is mainly due to the inherent continuity of the physical optics components contributing to the backscattered field of TD-ITD. Essentially, the physical optics solution, unlike the geometrical optics one, is continuous at the reflection shadow boundaries. This is true even without taking into consideration the diffraction due to the edge or the shadow boundary line. The plots in Fig. 3 show that the main contribution to the backscattered field is due to the physical optics component. The field plotted in Fig. 3a, which is magnified by a factor of eighty, illustrates that contributions due to scattering from the shadow boundary line and the edges are negligible by comparison to the physical optics part. One should also note that unlike the fields resulting from the application of TD-UTD [17], the fields shown in Figs. 2 and 3 are free of singularities that appear at the caustics.

Another feature displayed by TD-ITD calculations is the existence of a noticeable field trailing behind the main scattered wavefront. The same effect has been noted in relation to the scattering of pulsed plane waves from a circular disk. In contrast, this trailing part of the backscattered field has not appeared in calculations using TD-UTD. The reason for the existence of such a trailing field has been discussed in Refs. [16] and [25]. The behavior of the backscattered X-wave of Fig. 2a, as it moves away from the scattering circular disk, is illustrated in Fig. 4. The fields plotted at $t = 8$ and $10\,\mathrm{ns}$ show that at farther distances from the disk, the shape of the scattered field starts changing from that of a localized X-wave to that of a spherical wave.
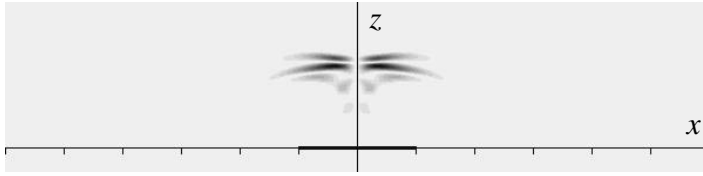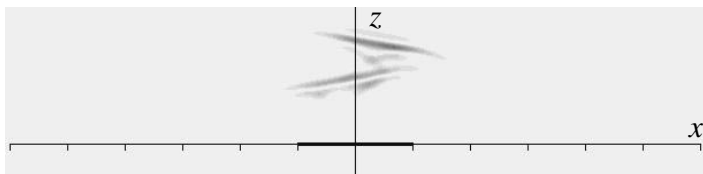
a. $(x_0 = 0, y_0 = 0, z_0 = 110 \, \text{cm})$
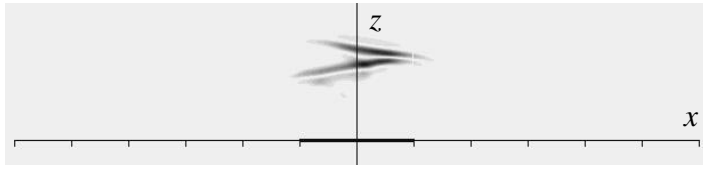
b. $(x_0 = 50 \, \text{cm}, y_0 = 0, z_0 = 110 \, \text{cm})$
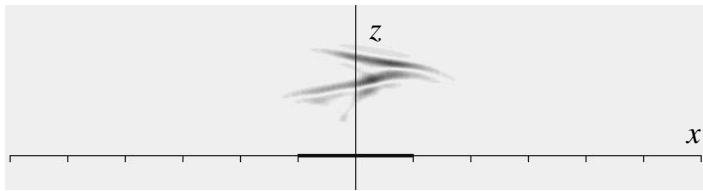
c. $(x_0 = 75 \, \text{cm}, y_0 = 0, z_0 = 110 \, \text{cm})$

d. $(x_0 = 100 \, \text{cm}, y_0 = 0, z_0 = 110 \, \text{cm})$

Figure 2. The total backscattered field of a TE X-wave (ϕ component) incident normally on a perfectly conducting circular disk of radius $L = 50 \, \text{cm}$ at time $t = 6 \, \text{ns}$. The parameters characterizing the incident X-wave are $a_0 = 10 \, \text{cm}$ and $\theta_0 = 10°$. The plots are calculated for different initial ($t = 0$) reference points (x_0, y_0, z_0): **a.** (0, 0, 110 cm), **b.** (50, 0, 110 cm), **c.** (75, 0, 110 cm) and **d.** (100, 0, 110 cm).
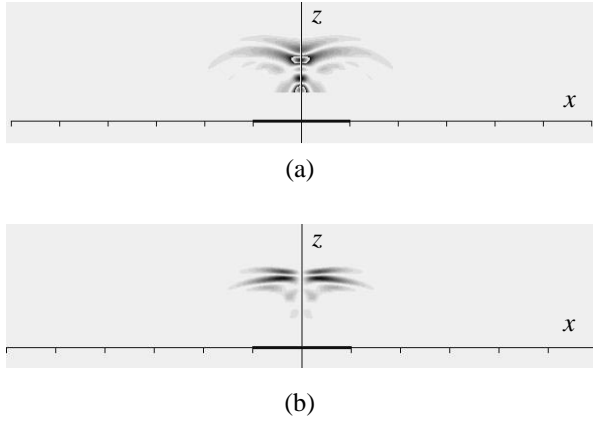
(a)

(b)

Figure 3. (a) Edge-diffracted and (b) physical optics parts of the total field (ϕ component) corresponding to Fig. 2a. The two fields are normalized to the peak value of the incident TE X-wave. The amplitude of the field in (a) is multiplied by a factor of eighty.
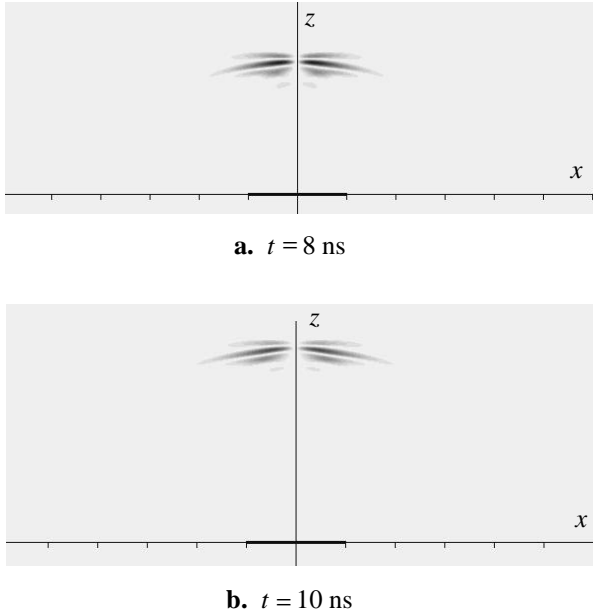

a. $t = 8$ ns

b. $t = 10$ ns

Figure 4. Total E_ϕ field in the backscattering region of a TE X-wave normally incident on a perfectly conducting circular disk at $t = 8$ and 10 ns. All parameters are the same as in Fig. 2a.
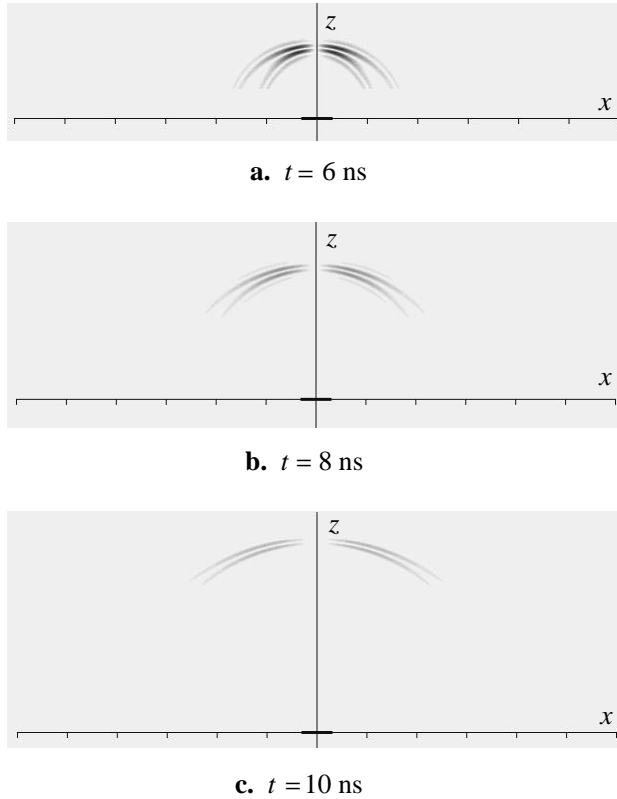
a. $t = 6$ ns

b. $t = 8$ ns

c. $t = 10$ ns

Figure 5. Total E_ϕ field in the backscattering region of a TE X-wave normally incident on a perfectly conducting circular disk of radius $L = 15$ cm at different observation times. The reference point at $t = 0$ is $(x_0, y_0, z_0) = (0, 0, 110\,\text{cm})$. The parameters of the incident X-wave are $a_0 = 10$ cm and $\theta_0 = 10°$. The plotted field is normalized to the peak of the incident TE X-wave and multiplied by a factor of five.

Such behavior can be emphasized either by increasing the distance traveled by the backscattered field or by decreasing the diameter of the disk, as shown in Fig. 5, where the radius is reduced to $L = 15$ cm. Again, this behavior is more realistic than the preservation of the plane wavefronts displayed by TD-UTD calculations.

5. FOUR-SENSOR CORRELATED DETECTION OF X-WAVES SCATTERED FROM A CIRCULAR DISK

It has been shown in the previous section that the scattered field due to a TE X-wave normally incident on a finite scattering structure becomes a spherical wave in the far region. Such behavior indicates that the backscattered field loses the initial localization of the incident X-wave at farther distances from the scattering object. Therefore, the localization property of the X-wave is essentially useful for focusing the incident wavefield on the scattering target. For the backscattered X-wave field, there is another important property that can be useful for detection schemes. Specifically, the X-wave is azimuthally symmetric around its center of localization with respect to its axis of propagation. This symmetry can be retained in the scattered field of the X-wave which is symmetrically incident on the disk. We suggest that in order to detect such a field symmetry in two orthogonal directions, at least four electric dipoles should be arranged on the circumference of a circle whose axis coincides with the axis of the incident X-wave. Although the ideas considered in this section apply to a large number of dipoles, we choose to discuss them in relation to four sensors only. If the localization region of a normally incident X-wave strikes an axially symmetric portion of the scattering structure, the reflected signals detected by the four sensors will have the same shape at the same time. The four-sensor scheme advocated here is based on multiplying the amplitudes of the signals detected by the four dipoles. Consequently, if the four dipoles capture the same signal at the same time there is a non-zero total output. On the other hand, if one or more of these sensors do not receive a signal, then the multiplied level of the four-dipoles becomes equal to zero. Similarly, if one or more of the detected signals is shifted in time by a period more than the temporal width of the captured signal, the total output reduces to zero. For a more practical detection scheme, however, one has to allow for deviations from perfectly symmetric scatterers. Therefore, slight temporal delays should be accounted for using signal-processing techniques. One should also be aware that although this concept can be generalized for a larger number of sensors, correlated detection of the backscattered signal by multiple sensors may become very sensitive, thus reducing the reliability of this method.

The most appropriate radius of the four-sensor circle, where the signal detected by each sensor attains maximum value, is equal to the height of the sensors above the scattering structure multiplied by $\tan \theta_0$. Therefore, the separations between the sensors become impractical for large detection heights. To demonstrate the

effectiveness of the proposed detection scheme, we assume that the four sensors are arranged around the azimuthal ϕ direction on a circle of a diameter equal to one meter. The field is to be detected at a height of thirty meters above the scattering structure. The normal axis of symmetry of the four sensors is adjusted to coincide with the axis of the incident X-wave. The common axis of the X-wave and the four sensors move transversally and the multiplied-output signal of the four-sensors is plotted as a function of time at each transverse observation point. The observed field is characterized by spherical wave fronts with spreading factors proportional to $1/r$. Thus, the field detected by each dipole is normalized to the peak value of the incident X-wave and is multiplied by the distance r from the scattering object. The resulting signal amplitude is multiplied by an additional factor to eliminate the spreading effect. This factor is of the order unity for a small scattering structure and decreases gradually for increasing dimensions of the scattering structure. Fig. 6 shows the four-sensor output for a normally incident first order TE X-wave as a function of time and space for scattering disks of different radii. The parameters of the incident X-wave are $a_0 = 10\,\mathrm{cm}$ and $\theta_0 = 10°$. The field distribution of the incident TE X-wave is the same as shown in Fig. 1. For such parameters, the localization region is at $\rho_{MAX} \approx 21\,\mathrm{cm}$ from the axis of the X-wave. The horizontal scale in Fig. 6 represents the x-axis and the vertical axis represents the observation time. The horizontal scale is divided into steps of $10\,\mathrm{cm}$. The predicted observation time is the time taken by the X-wave to travel from its starting point to the scattering body plus the time for the backscattered spherical wave to reach the detectors. The starting and the detection points are at a height of thirty meters above the scattering body. In this case, the predicted observation time is equal to $t_{obs} = (z_0/(c/\cos\theta_0)) + (z_0/c) \approx 198.5\,\mathrm{ns}$. Consequently, the time axis in Fig. 6 starts at $t = 195\,\mathrm{ns}$ and ends at $t = 202\,\mathrm{ns}$, so that the predicted observation time lies at the center of the time axis.

The field captured by each dipole of the four sensors is calculated using the time-domain incremental theory of diffraction. It should be noted that for scattering disks with radii smaller than the four-sensors output is localized above the edges of the disk as shown in Figs. 6a and 6b, where the radii of the scattering disks equal 15 and $20\,\mathrm{cm}$, respectively. This can be explained in terms of the null in the field of the incident TE X-wave along its axis of propagation. Thus, when the center of the incident X-wave coincides with the center of the scattering disk, the disk is illuminated by the weak central part of the X-wave localization region. However, as the axis of the incident X-wave moves slightly away from the axis of the scattering disk, half of the
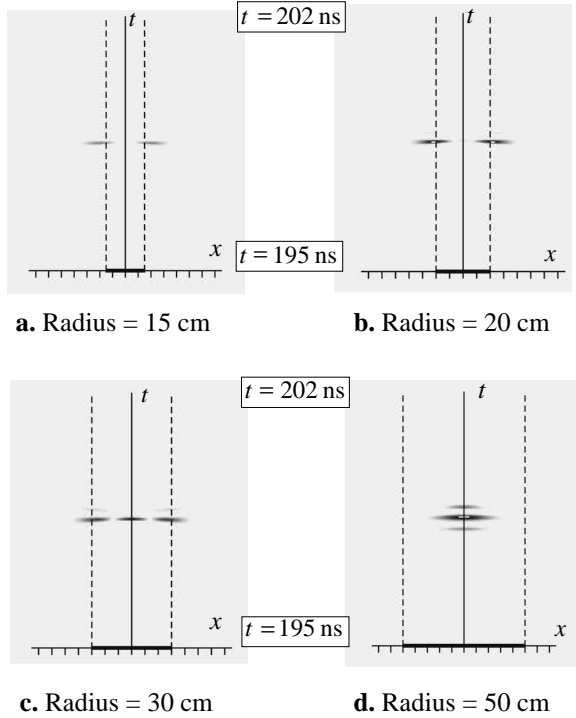
a. Radius = 15 cm   b. Radius = 20 cm

c. Radius = 30 cm   d. Radius = 50 cm

Figure 6. Four-sensor multiplied output of the backscattered fields due to a first order TE X-wave normally incident on a perfectly conducting disk. The observed signal is plotted as a function of x and t for disks of different radii. The time scale starts at $t = 195$ ns and ends at $t = 202$ ns. Each division in the x-direction represents 10 cm. The parameters of the incident X-wave are $a_0 = 10$ cm and $\theta_0 = 10°$. The localization center at time $t = 0$ is located at $(x_0 =$ variable, $y_0 = 0,\ z_0 = 30$ cm). The center of the four-sensor detector coincides with the localization center at $t = 0$ and x_0 varies from -75 cm to $+75$ cm.

localized region illuminates the disk. Thus, the scattered field in this case is increased. Due to the obliqueness of the arms of the X-wave [cf. Fig. 1], the field distribution on the disk is not uniform. Consequently, the outputs of the four sensors coincide only in a very short period as shown in Fig. 6a. The output of each sensor is normalized to the peak value of the incident X-wave and is multiplied by the distance $r \approx z_0$ to eliminate the spherical spreading effect. To quantify the directivity of the scattered signal at the sensors, an additional multiplication factor

is used. The multiplication factor is chosen to make the maximum value of the four-sensor output multiplied by the distance z_0 equal nearly the peak value of the incident X-wave. This factor can be used as a measure for the decay of the four-sensor output as the dimension of the scattering body is decreased. In Fig. 6a, where the radius of the disk is 15 cm, the additional multiplication factor is nearly 12.6. In Fig. 6b, where the radius of the disk is increased to 20 cm, the additional multiplication factor is reduced to be nearly 7.2. In Fig. 6c, the radius of the disk is increased to 30 cm and the multiplication factor is reduced to be 3.3. In this case, it can be pointed out that the detected output of the four-sensor scheme is localized above the edges of the disk as well as above its center. The localization above the edges can be explained following the same line of reasoning as in Figs. 6a and 6b. The detected localized field appears above the center when the radius of the scattering disk becomes slightly larger than $\rho_{\max}$, the location of the maximum field of the incident X-wave. In this case, the axis of the incident X-wave coincides with the axis of the scattering disk and the outer parts of the disk are illuminated by a high intensity field that can then be detected simultaneously by the four sensors. Fig. 6d shows the four-sensor observed signal for a disk of radius $R = 50$ cm. The additional multiplication factor in this case is reduced to 1.2. It should be noted in this case that the observed field is only concentrated over the center of the scattering disk. This is due to the fact that the localization region of the incident wave is completely reflected by the disk when the axis of the incident X-wave coincides with the axis of the circular disk. Consequently, the observed field attains a large value when the axis of localization lies above the center of the disk. The observed field near the edges in this case is negligible in comparison to the field detected at the center. When the axis of the X-wave is near the edge, the field distribution along the disk is nonuniform, causing the fields detected by the four dipoles to be separated in time so that the multiplied output of the four-sensor scheme becomes negligible.

6. RESOLVING POWER OF THE FOUR-SENSOR SCHEME FOR AN INCIDENT TE X-WAVE

The plot in Fig. 7 shows the output of the four-sensor arrangement for the case of two scattering circular disks of radii $L = 15$ cm separated by 100 cm. All the other parameters are the same as in Fig. 6a. The multiplied output of the four sensors is plotted as a function of time as the centers of both the incident X-wave and the four-sensor arrangement move in the x-direction. By comparing Figs. 7
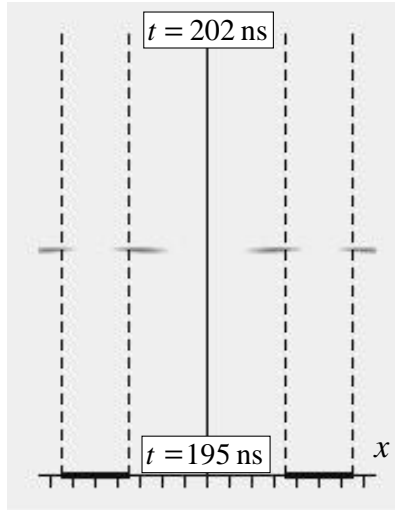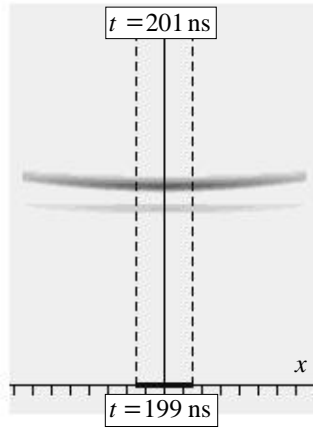
Figure 7. Four-sensor multiplied output of the backscattered fields due to a TE X-wave normally incident on two perfectly conducting disks of radii $L = 15$ cm and separated by 100 cm. The other parameters are identical to those used in Fig. 6.

and 6a, it can be seen that the received signal due to each disk is completely separated from that of the other. Such behavior is due to the localization of the incident X-wave and constitutes the main advantage for using the four-sensor scheme together with an incident X-wave in high-resolution detection applications.

To emphasize the advantage of using an X-wave, the four-sensor scheme is applied to a normally incident pulsed plane wave scattered both by one and two disks. The field captured by each dipole of the four sensors is calculated using the time-domain incremental theory of diffraction [25]. The backscattered field measured by the four dipoles is shown in Fig. 8. To simplify the comparison, the radii of the disks are $L = 15$ cm, as in Figs. 6a and 7. The incident pulsed plane wave is characterized by a spectral function $E_0(\omega) = \exp[-a_0\omega/c]$, with $a_0 = 3$ cm. The peak of the wavefront of the pulsed plane wave at time $t = 0$ is assumed to be at a height $z_0 = 30$ m above the plane of the scattering disks, the same as the position of the four-sensor detector. Thus, the predicted observation time is approximately given by $t = 2z_0/c = 200$ ns. The observed signal due to the scattering of the pulsed plane wave is plotted in time in the range from 199 to 201 ns. In the present case, the incident field is not characterized by a

a. A single scattering disk of radius 15 cm.

b. Two perfectly conducting disks of
radii 15 cm and separated by 100 cm.

Figure 8. Four-sensor multiplied output of the detected fields due to
a normally incident pulsed plane wave. The observed signal is plotted
as a function of x_0 and time. The time scale starts at $t = 199$ ns and
ends at $t = 201$ ns. The spectrum of the incident pulsed plane wave
is $E_0(\omega) = \exp[-a_0\omega/x]$, with $a_0 = 3$ cm. The peak of the incident
pulsed wave at time $t = 0$ is located at $z_0 = 30$ m. The center of the
four-sensor detector is located at ($x_0 = $ variable, $y_0 = 0$, $z_0 = 30$ m),
x_0 varies from -75 cm to $+75$ cm.

reference point along the x-axis. Thus, the observed signal is plotted as a function of moving the center of the four-sensor detector only along the x-axis. The spreading factor of the incident pulsed plane wave is unity. However, the backscattered field from a finite scattering body has a spherical wave form which decays as $1/z_0$. Consequently, the field of each of the four detector dipoles is normalized to the peak value of the incident pulsed plane wave and is multiplied by z_0 as in the case of the X-wave. An additional multiplication factor of 12.6 is also used to account for the area of the scattering structure as discussed in the case of an incident X-wave.

The multiplied detected signals of the four-sensor for the case of a single disk is shown in Fig. 8a. The time of the received signal is related to the transverse distance by a parabolic relation. This is a main feature of the usual ground penetrating radar (GPR) signal due to a finite scattering body. In the region above the scattering structure, where $x \ll z_0$, the transverse distance can be approximated by the parabolic relation $d_1 = z_0(1 + 0.5x^2/z_0^2)$. The intensity of the four-sensor output decreases when the center of the sensors is far from the center of the scattering disk due to the increase in the time shifts between the four detected signals. By comparing Figs. 8a and 6a, it can be seen that the measured output due to a pulsed plane wave is strong over a transverse distance much larger than the radius of the scattering disk. On the other hand, the output of the X-wave is limited to the extension of the disk and displays an exceptional capacity for detecting the position of the edge of the scatterer.

Fig. 8b shows the multiplied output of the four sensors for the case of two identical disks separated by 100 cm and illuminated by a pulsed plane wave. In this situation, the discrimination between the two disks from the received signal is impossible. By comparing Figs. 8a and 8b, it can be concluded that the output shown in the second figure resembles the product of the four detected signals arising from a larger disk centered at the mid-distance between the two disks. This behavior is due to the small separation between the two disks relative to the distance of the observation point. For a smaller observation distance, the parabolic shape of the output due to each disk could be resolved. Comparing Figs. 8b and 7, one can clearly appreciate the higher resolving capability of X-waves over pulsed plane waves when using the four-sensor detection scheme. In particular, a system using X-waves can become particularly advantageous if the four-sensor detector is mounted on a platform hovering at a large distance over the scatterers.

7. CONCLUDING REMARKS

In this paper, the diffraction and scattering of a TE X-wave by circular disk has been investigated using the time-domain incremental theory of diffraction (TD-ITD). This technique was introduced in Ref. [25] and was applied to the scattering of a pulsed plane wave from a circular disk. The frequency-domain incremental theory of diffraction of a plane wave (ITD) was introduced by Tiberio et al. [21–23], who also formulated a time- domain version of the theory. However, their TD-ITD formulation utilized transition functions from the geometrical theory of diffraction. In contrast, the version of the TD-ITD expounded in Ref. [25] was based on the uniform theory of diffraction. In Ref. [25], as well as in this paper, it has been demonstrated that the TD-ITD can be extremely effective in dealing with the scattering of pulsed fields having a Laplace-type spectral content.

The TD-ITD analysis of the diffraction and scattering of a TE X-wave relies on the use of the pulsed plane wave representation of the X-wave introduced in Refs. [8, 16] and [26]. In this case, the diffraction and scattering of each pulsed plane wave component of the incident X-wave is calculated at the observation point. The azimuthal angular superposition of the diffracted and scattered pulsed plane wave components yields the diffracted and scattered field of the X-wave. The TD-ITD technique was developed mainly for studying the behavior of the backscattered field far from finite scattering structures and to estimate the relative importance of the edge-diffracted field compared with the physical optics reflected and transmitted parts of the total field. Comparing the results of TD-ITD obtained in this work to those derived on the basis of the TD-UTD [17], we find that the results of both techniques have common characteristics. The main difference between the results of the two techniques is that, away from the scattering body, the backscattered field changes into a spherical wave and gradually loses its initial localization. This behavior is absent from the results based on the TD-UTD. Furthermore, no singularities are formed at caustics when the TD-ITD is used to calculate the scattered field.

In order to make use of both the localization and symmetry properties of the incident field, four-sensor detection technique has been introduced. This scheme utilizes four detection electric dipoles located on the circumference of a circle whose axis coincides with the axis of the incident X-wave. The signals received simultaneously by the four sensors are multiplied. When the localization region is incident on the scattering structure, the signals detected by the four sensors are

registered at the same time. Thus, the output of the four-sensor system does not vanish in this case. However, if the incident localization region does not illuminate the scattering structure effectively, the signals detected by the four sensors are shifted in time, or some of the signals vanish completely. In this situation, the multiplicative output of the four sensors vanishes. Numerical results illustrating the effectiveness of the advocated four-sensor system have been presented. The response of the four-sensor output for an incident X-wave has been simulated. For the sake of comparison, the four-sensor detection scheme has also been applied to the case of an incident pulsed plane wave. It has been shown that for an incident pulsed plane wave, the output of the four sensors has very low resolution in comparison to the X-wave. This behavior emphasizes the effectiveness of X-waves for ultra-wideband radar applications.

REFERENCES

1. Brittingham, J. N., "Focus wave modes in homogeneous Maxwell equations: Transverse electric mode," *J. Appl. Phys.*, Vol. 54, 1179–1189, 1983.
2. Ziolkowski, R. W., "Exact solutions of the wave equation with complex source locations," *J. Math. Phys.*, Vol. 26, 861–863, 1985.
3. Ziolkowski, R. W., "Localized transmission of electromagnetic energy," *Phys. Rev. A*, Vol. 39, 2005–2033, 1989.
4. Ziolkowski, R. W., "Properties of electromagnetic beams generated by ultra-wide bandwidth pulse driven arrays," *IEEE Trans. Antennas and Prop.*, Vol. 40, 888–905, 1992.
5. Ziolkowski, R. W., D. Lewis, and B. Cook, "Evidence of localized wave transmission," *Phys. Rev. Lett.*, Vol. 62, 147–150, 1989.
6. Lu, J. and J. F. Greenleaf, "Nondiffracting X waves — Exact solutions to free-space scalar wave equation and their finite aperture realization," *IEEE Trans. on Ultrason. Ferroelect. Freq. Contr.*, Vol. 39, 19–31, 1992.
7. Lu, J. Y. and J. F. Greenleaf, "Experimental verification of nondiffracting X waves," *IEEE Trans. Ultrason. Ferroelec. Freq. Contr.*, Vol. 39, 441–446, 1992.
8. Saari, P. and K. Reivelt, "Evidence of X-shaped propagation-invariant localized light waves," *Phys. Rev. lett.*, Vol. 79, 4135–4138, 1997.
9. Reivelt, K. and P. Saari, "Optical generation of focus wave modes," *J. Opt. Soc. Am. A*, Vol. 17, 1785–1790, 2000.
10. Besieris, I. M., A. M. Shaarawi, and R. W. Ziolkowski, "A

bidirectional traveling wave representation of exact solution of the scalar wave equation," *J. Math. Phys.*, Vol. 30, 1254–1269, 1989.

11. Besieris, I., M. Abdel-Rahman, A. Shaarawi, and A. Chatzipetros, "Two fundamental representations of localized pulse solutions of the scalar wave equation," *Progress in Electromagnetics Research*, J. Kong (ed.), PIER 19, 1–48, EMW Publishing, Cambridge, MA, 1998.

12. Ziolkowski, R. W., I. M. Besieris, and A. M. Shaarawi, "Aperture realization of exact solution to homogenous-wave equations," *J. Opt. Soc. Am. A*, Vol. 10, 75–87, 1993.

13. Shaarawi, A. M., R. W. Ziolkowski, and I. M. Besieris, "On the evanescent fields and the causality of the focus wave modes," *J. Math. Phys.*, Vol. 36, 5565–5587, 1995.

14. Mugnai, D., A. Ranfagni, and R. Ruggeri, "Observation of superluminal behaviors in wave propagation," *Phys. Rev. Lett.*, Vol. 84, 4830–4833, 2000.

15. Recami, E., "On localized X-shaped superluminal solutions to Maxwell's equations," *Physica A*, Vol. 252, 586–610, 1998.

16. Attiya, A. M., "Transverse (TE) electromagnetic X-waves: Propagation, scattering, diffraction and generation problems," Ph.D. Thesis, Cairo University, May 2001.

17. Attiya, A. M., E. El-Diwany, A. M. Shaarawi, and I. M. Besieris, "Diffraction of a transverse electric (TE) X wave by conducting objects," Accepted for publication.

18. Kouyoumjian, R. G. and P. H. Pathak, "A uniform geometrical theory of diffraction for an edge in a perfectly conducting surface," *Proc. IEEE*, Vol. 62, 1448–1461, 1974.

19. Rousseau, P. R. and P. H. Pathak, "Time-domain uniform geometrical theory of diffraction for a curved wedge," *IEEE Trans. Antennas and Prop.*, Vol. 43, 1375–1382, 1995.

20. Capolino, F. and R. Tiberio, "A time-domain incremental theory of diffraction (TD-ITD) for a wedge," *Proceedings of the International Conference on Electromagnetic in Advanced Application (ICEAA 01)*, Torino, Italy, September 10–14, 2001.

21. Tiberio, R. and S. Maci, "An incremental theory of diffraction: scalar formulation," *IEEE Trans. Antennas and Prop.*, Vol. 42, 600–611, 1994.

22. Tiberio, R., S. Maci, and A. Toccafondi, "An incremental theory of diffraction: Electromagnetic formulation," *IEEE Trans. Antennas and Prop.*, Vol. 43, 87–96, 1995.

23. Maci, S., R. Tiberio, and A. Toccafondi, "Incremental diffraction

coefficients for source and observation at finite distances from an edge," *IEEE Trans. Antennas and Prop.*, Vol. 44, 593–599, 1996.

24. Fagerholm, J., A. Friberg, J. Huttunen, D. Morgan, and M. Salomaa, "Angular-spectrum representation of nondiffracting X waves," *Physical Rev. E*, Vol. 54, 4347–4352, 1996.

25. Attiya, A. M., E. El-Diwany, A. M. Shaarawi, and I. M. Besieris, "A time-domain incremental theory of diffraction: scattering of electromagnetic pulsed plane waves," submitted to the same journal.

26. Attiya, A. M., E. A. El-Diwany, A. M. Shaarawi, and I. M. Besieris, "Reflection and transmission of X-waves in the presence of planarly layered media: The pulsed plane wave representation," *Progress in Electromagnetics Research*, J. Kong (ed.), PIER 30, 191–211, EMW Publishing, Cambridge, MA, 2000.

27. Jordan, E. C. and K. G. Balmain, *Electromagnetic Waves and Radiating Systems*, Prentice-Hall, New Delhi, 1974.

28. Gradshteyn, I. S. and I. M. Ryzhik, *Table of Integrals, Series and Products*, Fifth Edition, Academic Press, Boston, 1994.